Chapter 6

Assessment of the new non-local methodology complementing existing local methods

In this chapter, the non-local methodology for the study of the geometry of structures in turbulence introduced in Chapter 2 and used in Chapter 5 is utilized to complement two local criteria present in the literature for the identification of vortex tubes and vortex sheets in turbulent flows. The purpose is to provide a qualitative and quantitative assessment of the geometrical aspects of those local identification criteria. This is performed by applying the non-local methodology to confirm whether the educed structures show the expected geometries. The local and non-local methods are applied to the same numerical database referred to in Chapter 5.

6.1 Local identification criteria

Among the various local criteria found in the literature, here we consider those used in Horiuti & Takagi (2005) and HF for educing vortex tubes and sheets, which are outlined below. A point is considered to belong to a vortex tube core where the second invariant, Q, of the velocity gradient tensor, $\partial u_i/\partial x_j$, has a *sufficiently* large value. Q is defined as:

$$Q \equiv \frac{1}{2}\left[\left(\frac{\partial u_i}{\partial x_i}\right)^2 - \frac{\partial u_i}{\partial x_j}\frac{\partial u_j}{\partial x_i}\right]. \tag{6.1}$$

For incompressible flow, $\partial u_i/\partial x_i = 0$, and Q is related to $\omega_i\omega_i$ and $S_{ij}S_{ij}$ by:

$$2\,Q = -\frac{\partial u_i}{\partial x_j}\frac{\partial u_j}{\partial x_i} = \Omega_{ij}\Omega_{ij} - S_{ij}S_{ij} = \frac{1}{2}\,\omega_i\omega_i - S_{ij}S_{ij} \tag{6.2}$$

The condition $Q > 0$ was first used by Hunt et al. (1988), in combination with the additional constraint of the pressure, p, being lower than ambient, to define vortex tubes. The Poisson's equation for pressure in incompressible turbulent flow with density ρ can be rewritten as (see Bradshaw & Koh, 1981):

$$\frac{1}{\rho}\frac{\partial^2 p}{\partial x_i \partial x_i} = -\frac{\partial u_i}{\partial x_j}\frac{\partial u_j}{\partial x_i} = 2\,Q = \frac{1}{2}\,\omega_i\omega_i - S_{ij}S_{ij} \tag{6.3}$$

Therefore, Q is a pressure source term. Also, from the latter equality, enstrophy acts as a source term while dissipation acts as a sink term of pressure. There are some situations in which the Q-criterion is not adequate for educing vortex tubes, as is shown in Jeong & Hussain (1995) (e.g., conically symmetric vortex, axisymmetric axial vortex within a vortex ring, Bödewadt vortex).

For educing vortex sheets, the method proposed by Horiuti & Takagi (2005) is used in this chapter. At any given point, the eigenvalues of the symmetric second-order tensor $A_{ij} \equiv S_{ik}\Omega_{kj} + S_{jk}\Omega_{ki}$ are reordered as $[A_{ij}]_\omega$, $[A_{ij}]_+$, and $[A_{ij}]_-$. $[A_{ij}]_\omega$ is the eigenvalue whose corresponding eigenvector is most aligned with the vorticity field, ω_i, at that point. $[A_{ij}]_+$ and $[A_{ij}]_-$ are the remaining largest and smallest eigenvalues (in an algebraic sense), respectively. The eigenvalues, ϑ, of A_{ij} can be obtained from the depressed cubic equation:

$$\vartheta^3 - \frac{1}{2}A_{ij}A_{ji}\,\vartheta + \frac{1}{3}A_{ij}A_{jk}A_{ki} = 0. \tag{6.4}$$

Note that there is no term in ϑ^2 for being $A_{ii} = 0$, due to the symmetry of S_{ij} and antisymmetry of Ω_{ij}. Iso-contours of $[A_{ij}]_+$ are considered vortex sheets. This method takes advantage of the known feature of vortex sheets in which strain rate and vorticity are both large and correlated, reflected in $[A_{ij}]_+$. Horiuti & Takagi (2005) explain the advantages of this identification criterion over previously existing ones also based on that feature of vortex sheets (see, for example, Tanaka & Kida, 1993).

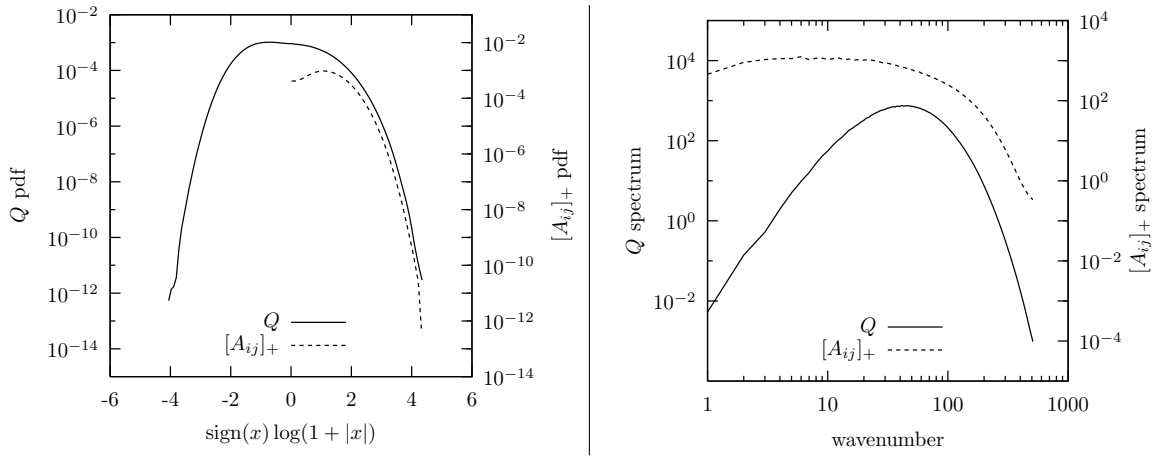

Figure 6.1: Volume pdfs in physical domain (left) and spectra in Fourier domain (right) of Q and $[A_{ij}]_+$ fields for the 1024^3 grid resolution. Note that the volume pdfs use a transformation of the form $\text{sign}(x)\log(1+|x|)$ in the abscissa coordinate, and that curves for Q and $[A_{ij}]_+$ fields use two different vertical axes (both in the pdfs and the spectra), shifted one decade for a clear view (non-intersecting curves)

6.2 Application of non-local methodology

Once the sets of iso-surfaces of Q and $[A_{ij}]_+$ are obtained, the non-local methodology introduced in Chapter 2 is applied to both sets. The multi-scale decomposition is not used in the extraction step, since the purpose is to assess the geometrical character of the iso-surfaces extracted by the local criteria. A multi-scale decomposition of the Q and $[A_{ij}]_+$ scalar fields could be applied beforehand (as was done for $\omega_i\omega_i$ and $S_{ij}S_{ij}$ in Chapter 5), and then iso-contours of the component fields could be independently obtained, but the meaning of the educed structures would not be the same as those obtained by iso-contouring the original fields of Q and $[A_{ij}]_+$, and the purpose of the assessment of the local criteria would be lost. While the three grid resolutions are available also for Q and $[A_{ij}]_+$ fields, only the finest (i.e., 1024^3) is used, since this chapter is not intended to evaluate the effect of the grid resolution in Q and $[A_{ij}]_+$ structures.

Figure 6.1 shows plots of the volume pdfs (left) and the spectra (right), in Fourier space, of the two fields, Q and $[A_{ij}]_+$, for that finest grid resolution (1024^3). The two plane cuts in Figure 6.2 correspond to Q (left) and $[A_{ij}]_+$ (right) fields, and were obtained normally to one of the principal directions of the cubic domain at half the side length. Iso-surfaces of Q and $[A_{ij}]_+$ extracted at contour values equal to the mean plus 5 and 4 times, respectively, the standard deviation of each

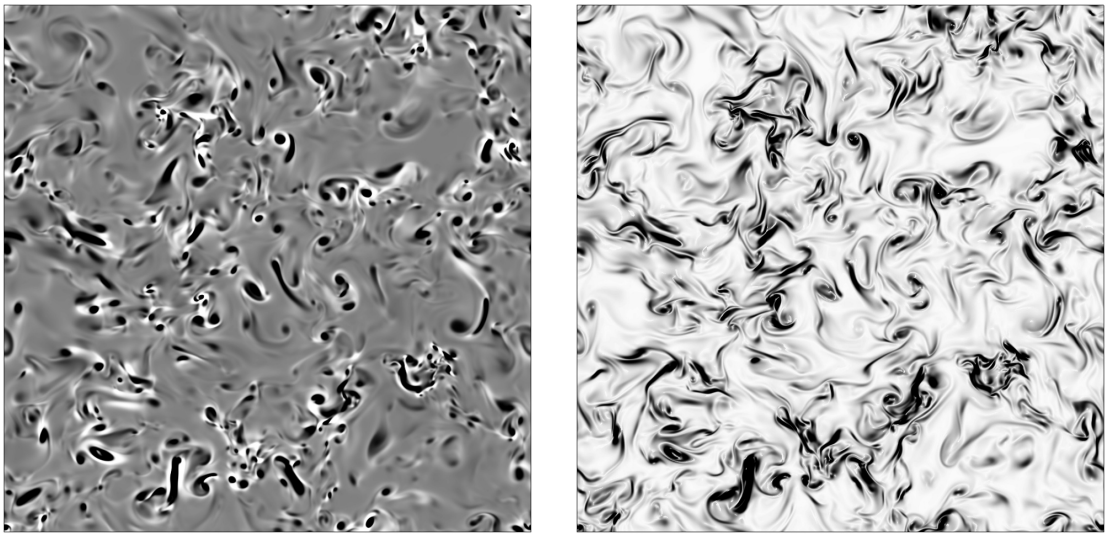

Figure 6.2: Plane cuts of Q (left) and $[A_{ij}]_+$ (right) fields normal one of the principal directions of the cubic domain, at half its side length

field are presented in Figure 6.3. These contour values are approximately the same ones used in HF (1200 for Q and 1000 for $[A_{ij}]_+$) to educe vortex tubes and sheets. The visualization spaces in Figure 6.4 contain glyphs corresponding to the geometrical characterization of the individual structures shown in Figure 6.3, with the same coloring scheme (blue used for Q structures and red for $[A_{ij}]_+$ structures). It is observed that structures of Q tend to be located near the $(\hat{S}, \hat{C}) = (1/2, 1)$ region, where tube-like structures are generally located, and present moderate-to-high stretching. On the contrary, $[A_{ij}]_+$ structures appear much closer to the $\hat{C} = 0$ region, thus corresponding to more planar geometries (sheet-like), and with lower values of λ, implying more stretched structures.

The clustering algorithm described in the classification step of the non-local methodology is applied to the set of structures formed by the union of both sets of iso-surfaces of Q and $[A_{ij}]_+$ fields, without any a priori distinction of structures of those two sets. This means that the algorithm has no knowledge of whether individual structures were extracted from Q or $[A_{ij}]_+$ fields. Owing to the equivalent number of structures educed for Q and $[A_{ij}]_+$ and the similar standard deviations of each population, the pre-clustering stratified random sampling with disproportionate allocation in this case results in practically the union of the complete sets. Then, structures are clustered based solely on their geometrical characterization given by set of parameters $\{\hat{S}, \hat{C}, \lambda, d_u^S, d_l^S, d_u^C, d_l^C\}$, that

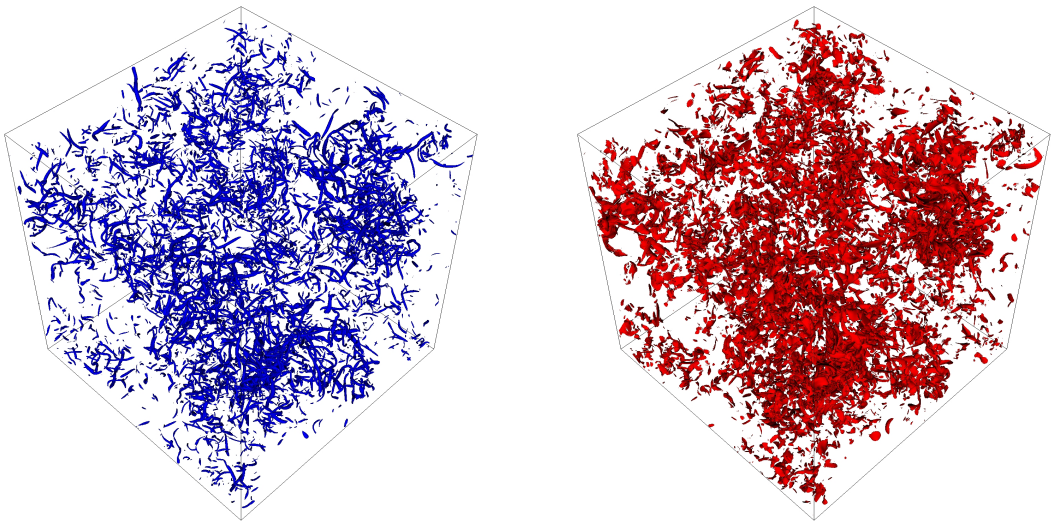

Figure 6.3: Iso-contours of Q and $[A_{ij}]_+$ fields extracted at their mean plus 5 and 4 times their standard deviation, respectively

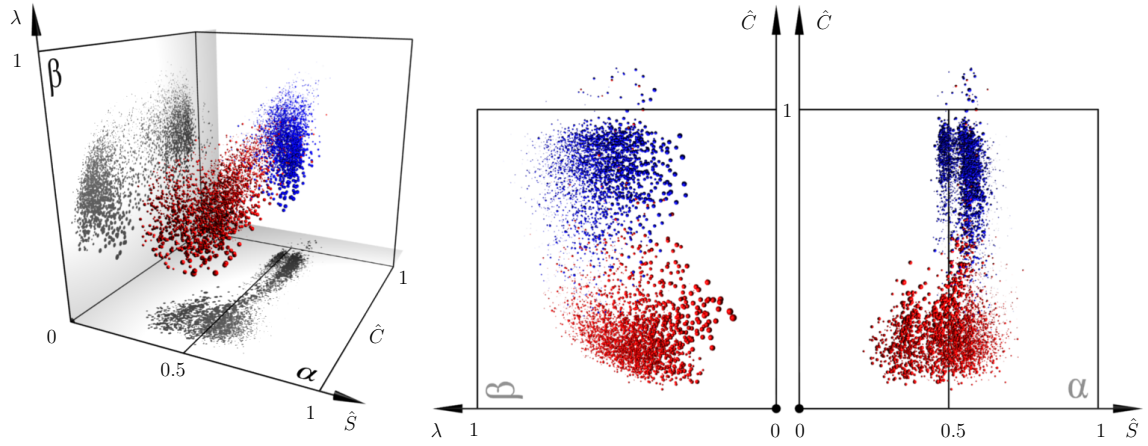

Figure 6.4: Visualization space—3D view (left) and lateral (center) and top (right) projections—with glyphs (spheres) representing educed structures of Q (blue) and $[A_{ij}]_+$ (red), scaled by the lognormalized area of each corresponding structure

define the feature space described in §2.3.2. An optimum number of clusters of 2 was found (see Figure 6.6), and the resulting clusters are shown in Figure 6.5, where each color corresponds to a different cluster. Glyphs (spheres) in that figure are scaled by the normalized silhouette coefficient, a measure of the degree of membership of each structure to the cluster it was assigned. Comparing Figures 6.5 and 6.4, it is confirmed that the two educed clusters correspond in their majority to the two sets of structures (Q and $[A_{ij}]_+$). Numerically a matching of 96% between pairs of groups was

obtained. A small percentage of structures of both fields shows a different geometry than the one expected according to the local criterion. For example, the central tube in Figure 7.5 (discussed later) is a structure of $[A_{ij}]_+$, which is meant to educe sheet-like structures, while the other two tubes in that plot are structures of Q, as expected.

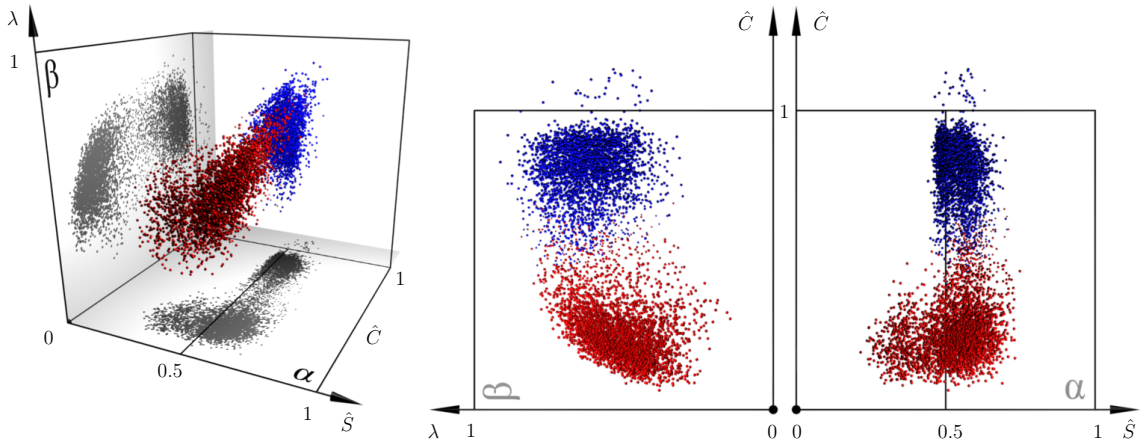

Figure 6.5: Clustering results in the visualization space—3D view (left) and lateral (center) and top (right) projections—with glyphs (spheres) representing optimum clusters of structures educed from the set union of Q and $[A_{ij}]_+$ structures. Glyphs are scaled by the normalized silhouette coefficient, which indicates the degree of membership of that element to the assigned cluster

We emphasize that the scaling of the glyphs in Figures 6.4 and 6.5 is different. Figure 6.4 uses the lognormalized area of each structure, and thus it can be concluded, for both Q and $[A_{ij}]_+$ that more stretched structures are typically larger (in area): glyphs with lower values of λ (more stretched) are bigger in that figure. On the other hand, glyphs in Figure 6.5 are scaled by the silhouette coefficient of the corresponding structure as a result of the clustering algorithm: bigger glyphs imply larger silhouette coefficient and, therefore, a higher degree of membership to the cluster the structure was automatically assigned. This different scaling contributes to an apparent lower density of glyphs in Figure 6.4, when compared to Figure 6.5, since glyphs associated with small structures would be also small in the former, while they will appear larger in the latter, if they have a high silhouette coefficient.

Figure 6.6 shows the optimality scores found during the automatic determination of the number of clusters. It is observed that a number of clusters of 2 provides an optimality score near 0.7 (1.0 being

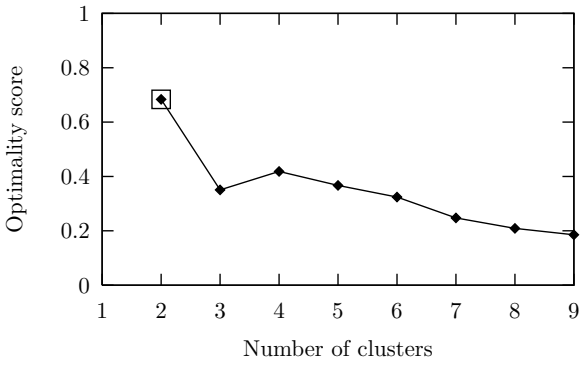

Figure 6.6: Optimality scores for different number of clusters obtained during the application of the clustering algorithm to the set of structures of Q and $[A_{ij}]_+$ together. An optimum number of clusters of 2 was automatically determined (square point)

the maximum), much higher, comparatively, than for other numbers of clusters. A comparison with the clustering results obtained for $\omega_i\omega_i$ and $S_{ij}S_{ij}$ in §5.5 (see Figure 5.14), where the optimality scores were rather low and the variation among different number of clusters was small, gives an indication of the higher level of confidence in the clustering results for this case. This could be anticipated by looking at the organization of glyphs in the visualization space in Figure 6.5, when compared to Figure 5.13.

Thus, the intuition that resulted by the visual cues of Figure 6.3 in which iso-surfaces of Q seemed tube-like and structures of $[A_{ij}]_+$ appeared sheet-like has been verified with a mathematical foundation first by the geometrical characterization, whose results can be partially seen in Figure 6.4, and then with the application of clustering techniques to the union of both sets, whose results are seen in Figure 6.5. The geometrical data can be used both qualitative and quantitatively.

Chapter 7

Interaction among structures of different fields: proximity issues

This chapter is devoted to the study of the interplay among structures of different fields under a geometrical perspective. We present here a methodology that, for each individual structure, performs an analysis of its proximal structures based upon their geometrical characterization previously introduced. Statistical results are obtained for the set of structures under study, presented in the form of combined probability density functions.

A motivation for this methodology is presented in §7.1, followed by the description of the methodology itself in §7.2. Results of its application to the four fields studied in previous chapters of this thesis grouped by pairs, namely Q–$[A_{ij}]_+$ and $\omega_i\omega_i$–$S_{ij}S_{ij}$, are presented in §7.3 and §7.4, respectively.

7.1 Motivation

The scalar fields that have been studied in the previous two chapters were all derived from the velocity gradient tensor. Some of them can be formulated in terms of the others by simple algebraic relations (e.g., Q in terms of $\omega_i\omega_i$ and $S_{ij}S_{ij}$). Other fields, not studied here but common in the study of turbulence, such as the pressure field, p, are also related to these (see equation 6.3). A passive scalar field could be also added to the flow and related to the other fields through the advection-diffusion equation, as we did in Chapter 4. They all can be thought of as different manifestations

of the same flow, in this case, incompressible homogeneous isotropic turbulence decaying in time in a periodic box. The mathematical relations among all of them are well known, and a vast effort has been dedicated in the fluid mechanics literature to study how those mathematical relations are translated into the physical aspects of turbulence, both in physical and Fourier domains, through the study of pdfs, structure and (auto-)correlation functions, spectra, etc.

It is thus conceivable that the structures extracted from those fields may have some relations, first, in their relative locations in physical space and, second, in their geometrical character, forming composite structures localized in physical domain. Perhaps the most common example of such inter-relation between scalar fields is the formation process of a vortex tube that results from the roll-up of a vortex sheet (see HF and the references therein): at an intermediate stage of that process, the core of the vortex tube is dominated by high values of vorticity, while the sheet that is rolling up around it presents high values of dissipation. Therefore, in that scenario, tube-like structures of $\omega_i\omega_i$ would be surrounded by sheet-like structures of $S_{ij}S_{ij}$. Similarly, considering the scalar fields used by the local identification criteria in §6.1 to educe vortex tubes and sheets, structures of Q (which were found to be tube-like) would be surrounded by structures of $[A_{ij}]_+$ (predominantly sheet-like).

Plane cuts of pairs of scalar fields, taken at the same location, are superimposed in Figure 7.1 ($S_{ij}S_{ij}$ over $\omega_i\omega_i$ on the left, $[A_{ij}]_+$ over Q on the right). Close relations between their corresponding structures are noticed: structures of $S_{ij}S_{ij}$ and $[A_{ij}]_+$ (red) tend to wrap around those of $\omega_i\omega_i$ and Q (blue), respectively. It is also observed that many structures of $\omega_i\omega_i$ and Q appear to have circular cores, while structures of $S_{ij}S_{ij}$ and $[A_{ij}]_+$ are more elongated. When extrapolated to the three-dimensional fields, those circular patches of the plane cuts of $\omega_i\omega_i$ and Q will likely belong to tubes, while the elongated regions of plane cuts of $S_{ij}S_{ij}$ and $[A_{ij}]_+$ will probably correspond to sheets around them. Another scenario in which circular and elongated regions of the plane cuts correspond, respectively, to blob-like and tube-like structures in three dimensions would be also possible, but its frequency of occurrence is comparatively smaller, as is concluded from the study of the geometry of the four fields previously done in Chapter 5. A methodology enabling study, in three dimensions, of the geometry of structures of different fields surrounding those of a particular field would be useful

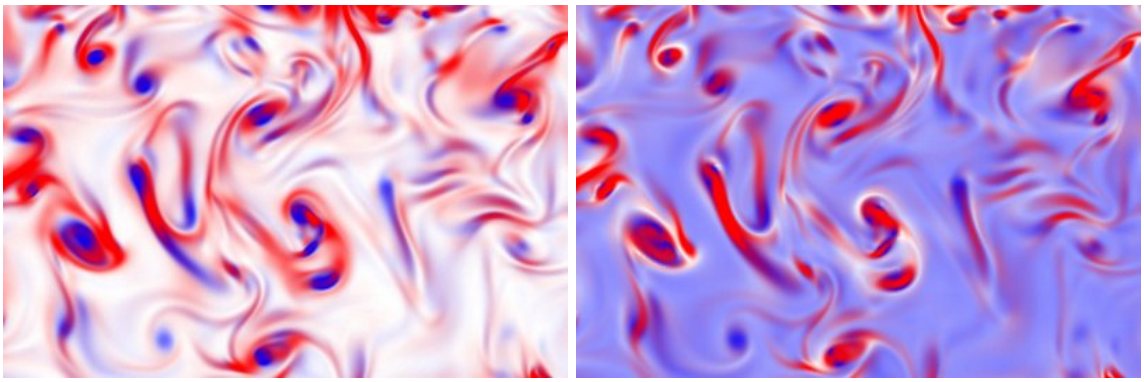

Figure 7.1: Left: Plane cut of $S_{ij}S_{ij}$ (red) superimposed over equivalent plane cut of $\omega_i\omega_i$ (blue). Right: Plane cut of $[A_{ij}]_+$ (red) superimposed over equivalent plane cut of Q (blue)

to test this visual intuition and to quantify its appearance.

7.2 Methodology

Consider two sets of structures, $\mathcal{A}$ and $\mathcal{B}$, containing $N_\mathcal{A}$ and $N_\mathcal{B}$ elements, respectively. We impose no Boolean restriction on both sets, so that elements of $\mathcal{A}$ can also be elements of $\mathcal{B}$.

7.2.1 Processing individual structures

For each structure $a_i \in \mathcal{A}$:

1. Obtain the subset $\mathcal{C}$ of $N_\mathcal{C}$ structures of $\mathcal{B}$ ($\mathcal{C} \subseteq \mathcal{B}$) that are closest to a_i in the bounding box sense. This step is intended to speed up the algorithm by reducing the load required to perform the rest of the steps.

2. For each $c_j \in \mathcal{C}$, $j = 1, ..., N_\mathcal{C}$, obtain the point-wise minimum distance map from c_j to a_i, $\text{MDM}(c_j, a_i)$. This map computes, for each point of the discretized surface c_j, the minimum of the distances from it to all points of a_i.

   At the same time, during the computation of $\text{MDM}(c_j, a_i)$, those points of a_i that provide the minima for $\text{MDM}(c_j, a_i)$ are tagged and an array of N_γ parameters is stored, for each one of those points, in a point-wise conditional array map of a_i, $\text{CAM}(a_i)$. The array of parameters $\{\gamma_k, k = 1, ..., N_\gamma\}$ contains, for each tagged point $P \in a_i$, the (dimensionless) proximity value,

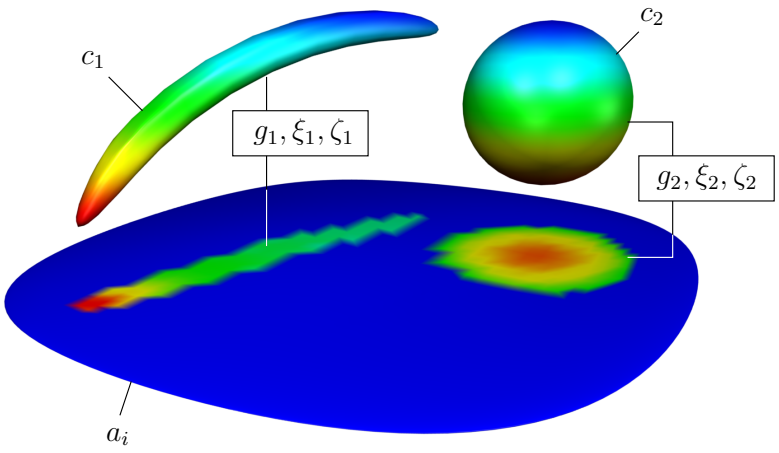

Figure 7.2: Schematic of the computation of the conditional array map (CAM) for a given structure a_i (sheet-like) with respect to two close structures c_1 (tube-like) and c_2 (blob-like). Minimum distance maps from c_j $(j = 1, 2)$ to a_i are shown, with a common color scale for both ranging from red to blue, representing smaller to larger minimum distances to a_i, respectively. The proximity value derived from them is mapped on a_i, with a color scale varying from blue (nil proximity) to red (maximum proximity). Those points of a_i tagged during the computation of the minimum distance maps (with proximity values greater than zero) will store also the values $\{g_j, \xi_j, \zeta_j\}$ of the corresponding c_j in the conditional array map

p, obtained from the minimum distance, d, to the point(s) of c_j for which P was the closest of all points in a_i, plus additional information of c_j itself (for example, but not limited to, an identifier of the structure c_j, and geometrical parameters of c_j obtained from a previous characterization performed on it). The dimensionless proximity, p, is defined in terms of the distance d by $p \equiv (1 + d/D_{a_i})^{-1}$, where D_{a_i} is a non-dimensionalizing length scale of a_i. Smaller distances, d, translate into higher proximity values ($p \in [0, 1]$).

We consider here the particular case in which, for each point P of a_i, the array $\{\gamma_k, k = 1, ..., N_\gamma\}$ consists of four parameters ($N_\gamma = 4$), redefined for simplicity as $\{p, g, \xi, \zeta\}_P$: p is the dimensionless proximity value to c_j described above, g is an index categorizing c_j among N_g known groups of structures present in $\mathcal{B}$, $\{G_g \subset \mathcal{B}, g = 1, ..., N_g \| \bigcup_{g=1}^{N_g} G_g = \mathcal{B}\}$ and ξ and ζ are geometrical properties of c_j. A schematic of the computation of the conditional array map for a_i based on the minimum distance maps for c_j is depicted in Figure 7.2.

As different c_j are processed, the conditional array map for a_i, CAM(a_i), is updated at previ-

ously untagged points of a_i. Also, the array of parameters of a previously tagged point of a_i is updated if the new proximity value for that point is larger than the previously stored one, meaning that the corresponding distance of the new structure c_j to that point is smaller than for all the previous c_j structures processed.

If c_j is the same structure as a_i, which can happen, since, as we stated above, $\mathcal{A}$ and $\mathcal{B}$ could share elements, then it is discarded in the computation of CAM(a_i). Otherwise it would eclipse all other structures of $\mathcal{C}$ and the conditional array map would be trivial and useless. Nevertheless, if c_j is not the same as a_i, but they happen to be identical, then c_j is included in the computation of CAM(a_i), resulting in a trivial but useful result. For example, if $\mathcal{A}$ and $\mathcal{B}$ are disjoint but their structures are identical by pairs $\{a_i, b_i\}$, the trivial CAM(a_i) obtained for each a_i after processing all structures $c_j \in \mathcal{C}$ would prove their identicality.

3. After all c_j have been processed for a given a_i we obtain, from the CAM(a_i), the joint probability density function (jpdf), in terms of p and g, based on area-coverage, denoted by $\mathcal{P}(p,g)\,|_{a_i \leftarrow \mathcal{C}}$. The value $\int_{p_1}^{p_2} \mathcal{P}(p,g)\,|_{a_i \leftarrow \mathcal{C}}\, \mathrm{d}p$ can be interpreted as the probability of finding structures of $\mathcal{C}$ categorized in a group G_g as being the closest structures to a_i in the range of proximity values $[p_1, p_2]$. At a given point $P \in a_i$, a structure c_{j^*} is the closest to a_i at P if it has the highest value of proximity, p, among all the structures c_j that would tag P in the computation of CAM(a_i).

   We compute also the area-based joint probability density function in terms of ξ and ζ, with an additional intensity component based on the averaged proximity value. For each 2D interval of the geometrical properties $[\xi_m, \xi_m + \Delta\xi] \times [\zeta_n, \zeta_n + \Delta\zeta]$ the discrete joint probability density function with intensity (jpdf+i) has two components: the first one is the pdf value itself, i.e., surface area of the a_i such that $(\xi, \zeta) \in [\xi_m, \xi_m + \Delta\xi] \times [\zeta_n, \zeta_n + \Delta\zeta]$ divided by the total area of a_i; the second component is the area-weighted average of the proximity values of all faces of the discretized a_i such that $(\xi, \zeta) \in [\xi_m, \xi_m + \Delta\xi] \times [\zeta_n, \zeta_n + \Delta\zeta]$. We denote that jpdf+i by $\vec{\mathcal{PI}}(\xi, \zeta; p)\Big|_{a_i \leftarrow \mathcal{C}}$, where the vector symbol reflects that it has two components (pdf in terms of $\{\xi, \zeta\}$ and intensity based on p).

We approximate:

$$[\mathcal{P}(p,g)|_{a_i \leftarrow \mathcal{B}} \approx [\mathcal{P}(p,g)|_{a_i \leftarrow \mathcal{C}}\,, \qquad \left[\vec{\mathcal{PI}}(\xi,\zeta\,;p)\right|_{a_i \leftarrow \mathcal{B}} \approx \left[\vec{\mathcal{PI}}(\xi,\zeta\,;p)\right|_{a_i \leftarrow \mathcal{C}}\,. \tag{7.1}$$

This approximation is exact when the structures of $\mathcal{C}$ eclipse, for $a_i \in \mathcal{A}$, structures of $\mathcal{B}-\mathcal{C}$, if $N_\mathcal{C} < N_\mathcal{B}$, and also in the trivial case $N_\mathcal{C} = N_\mathcal{B}$, for which it becomes an identity.

7.2.2 Transition from individual structures to results for the set $\mathcal{A}$

Once all $a_i \in \mathcal{A}$ have been processed, global jpdf and jpdf+i are obtained for the set $\mathcal{A}$ as the average of individual jpdf and jpdf+i for each a_i:

$$[\mathcal{P}(p,g)|_{\mathcal{A} \leftarrow \mathcal{B}} = \frac{\sum_{a_i \in \mathcal{A}} [\mathcal{P}(p,g)|_{a_i \leftarrow \mathcal{B}}}{N_\mathcal{A}} \tag{7.2}$$

$$\left[\vec{\mathcal{PI}}(\xi,\zeta\,;p)\right|_{\mathcal{A} \leftarrow \mathcal{B}} = \frac{\sum_{a_i \in \mathcal{A}} \left[\vec{\mathcal{PI}}(\xi,\zeta\,;p)\right|_{a_i \leftarrow \mathcal{B}}}{N_\mathcal{A}} \tag{7.3}$$

respectively. This is equivalent to assigning a probability density of $[\mathcal{P}(p,g)|_{a_i \leftarrow \mathcal{B}}\,/N_\mathcal{A}$ to each event $a_i \leftarrow \mathcal{B}$ and then computing the probability density of the event $\mathcal{A} \leftarrow \mathcal{B}$ as the union of all individual events ($\forall a_i \in \mathcal{A}$), taking them as independent. The same reasoning applies to $\left[\vec{\mathcal{PI}}(\xi,\zeta\,;p)\right|_{\mathcal{A} \leftarrow \mathcal{B}}$.

7.2.3 Computational remarks

When dealing with the discretized surfaces representing the structure a_i, $[\mathcal{P}(p,g)|_{a_i \leftarrow \mathcal{B}}\,/N_\mathcal{A}$ and $\left[\vec{\mathcal{PI}}(\xi,\zeta\,;p)\right|_{\mathcal{A} \leftarrow \mathcal{B}}$ are obtained from face-wise data, and not from point-wise data. This requires a transformation from point-wise to face-wise data, which is done in this case by assigning to each face the array $\{\gamma_k, k = 1, ..., N_\gamma\}$ of its vertex with the maximum value of the proximity (i.e., minimum distance). Interpolation, in this case, is inappropriate since there is no guarantee of continuity of the values of the parameters γ_k throughout the surface, as neighboring points can have data corresponding to different surrounding structures $c_j \in \mathcal{C}$. When continuity of the jpdf variables exists, an interpolation (for example, tri-linear if the faces are triangular) is justified and can improve

the accuracy of the jpdf, relaxing the dependence between the discretization of the surface and the discretization of the jpdf; this was the case in the computation of the $\mathcal{P}(S,C)$ used to obtain the signatures of the structures in the characterization step of the study of the non-local geometry of structures, but cannot be applied to the jpdf and jpdf+i we are analyzing in this chapter.

The algorithm can be modified to obtain directly face-wise data instead of point-wise data and avoid such transformation. Point-wise data has been chosen in our implementation due to the simplicity and increased speed when computing distance maps. Nonetheless, we note that this imposes the additional constraint that both discretized surfaces a_i and c_j must have an equivalent grid resolution for an accurate computation of the distance maps, basis of this algorithm. In our implementation, this is guaranteed as a consequence of the iso-contouring algorithm in use and the fact that, even when multi-scale techniques were applied, sub-sampling was not performed on the grid for any scale, and no decimating operation was applied over the discretized structures thereafter.

7.3 Application to structures of Q and $[A_{ij}]_+$

We apply the methodology explained in §7.2 to the structures of the fields Q and $[A_{ij}]_+$ educed in §6.1. In our first application, the set $\mathcal{A}$ will be composed of the extracted structures of Q, $\mathcal{A} \equiv \mathcal{X}(Q)$, where $\mathcal{X}(\alpha)$ denotes the set of extracted structures from a three-dimensional scalar field α, while the set $\mathcal{B}$ is composed of the union of structures extracted from Q and those extracted from $[A_{ij}]_+$, $\mathcal{B} \equiv \mathcal{X}(Q) \cup \mathcal{X}([Aij]_+)$. Therefore, in this particular case, $\mathcal{A} \subset \mathcal{B}$.

We choose (ξ, ζ) as the geometrical parameters $(\hat{S}, \hat{C})$ obtained in the characterization step of the non-local study of the geometry of structures applied in §6.2. The index g refers in this case to the two groups of structures in which $\mathcal{B}$ can be immediately divided, namely, structures of Q ($g = 1$) and structures of $[A_{ij}]_+$ ($g = 2$). The length scale D_{a_i} used to non-dimensionalize distances when computing proximity values for each structure a_i is taken to be the parameter $\mu \equiv 3\,V/A$, where V is the volume and A the area of a_i. Note that this parameter was used in the geometrical characterization step of Chapter 2 to non-dimensionalize the curvedness (see equation 2.6), resulting in the dimensionless value C, from which $\hat{C}$ was obtained. For a sphere of radius R, $\mu_{sphere} = R$;

for an elongated tube with circular cross section of radius R, $\mu_{tube} \approx 3\,R/2$; for a predominantly sheet-like structure of thickness t, $\mu_{sheet} \approx 3\,t/2$. After applying the methodology, we obtain both $\left[\vec{\mathcal{PI}}(\hat{S},\hat{C}\,;p)\right|_{\mathcal{A}\leftarrow\mathcal{B}}$ and $[\mathcal{P}(p,g)|_{\mathcal{A}\leftarrow\mathcal{B}}$.

7.3.1 Proximity and area coverage of surrounding structures through jpdf+i

Figure 7.3 shows $\left[\vec{\mathcal{PI}}(\hat{S},\hat{C}\,;p)\right|_{\mathcal{A}\leftarrow\mathcal{B}}$. The top left plot is the representation of the pdf component, using a greyscale, where white indicates nil area coverage and black indicates the maximum area coverage. Therefore, dark regions indicate that structures of $\mathcal{B}$ with values of $(\hat{S},\hat{C})$ within those regions are found, on average, to surround comparatively a larger proportion of the area of structures of $\mathcal{A}$. Light regions indicate values of $(\hat{S},\hat{C})$ not so commonly encountered in the structures of $\mathcal{B}$ surrounding those of $\mathcal{A}$. The top-right plot represents the intensity component, which in this case corresponds to the proximity value, using a color-scale (continuous gradient blue-cyan-green-yellow-red): blue indicates low proximity (farther distances) while red indicates high proximity (closer distances) of the structures of $\mathcal{B}$ with given values $(\hat{S},\hat{C})$ to those of $\mathcal{A}$. The bottom-left plot is a composition of both the pdf component and the intensity component by means of a hue-saturation gradient, represented in the bottom-right plot. In a HSB (hue, saturation, brilliance) color space, the area-coverage corresponds to the saturation, S, while the intensity component corresponds to the hue, H, and the brilliance, B, is kept constant at its maximum value. Therefore, it contains information of the averaged area-coverage in the saturation scale and information of the averaged proximity in the hue scale. Saturated-red regions correspond to values of $(\hat{S},\hat{C})$ found in structures of $\mathcal{B}$ closest to those of $\mathcal{A}$ and covering, comparatively, the largest proportion of their surface area. Desaturated regions indicate less area coverage and colors closer to the blue hue indicate lower values of the proximity (and thus, farther structures). Regions of saturated-blue, for example, will indicate that structures of $\mathcal{B}$ with those values of $(\hat{S},\hat{C})$ appear far but cover a large proportion of the surface area of structures of $\mathcal{A}$. Desaturated blue regions, on the other hand, will indicate that structures of $\mathcal{B}$ with those values of $(\hat{S},\hat{C})$ appear far as well, but covering a small fraction of the surface area

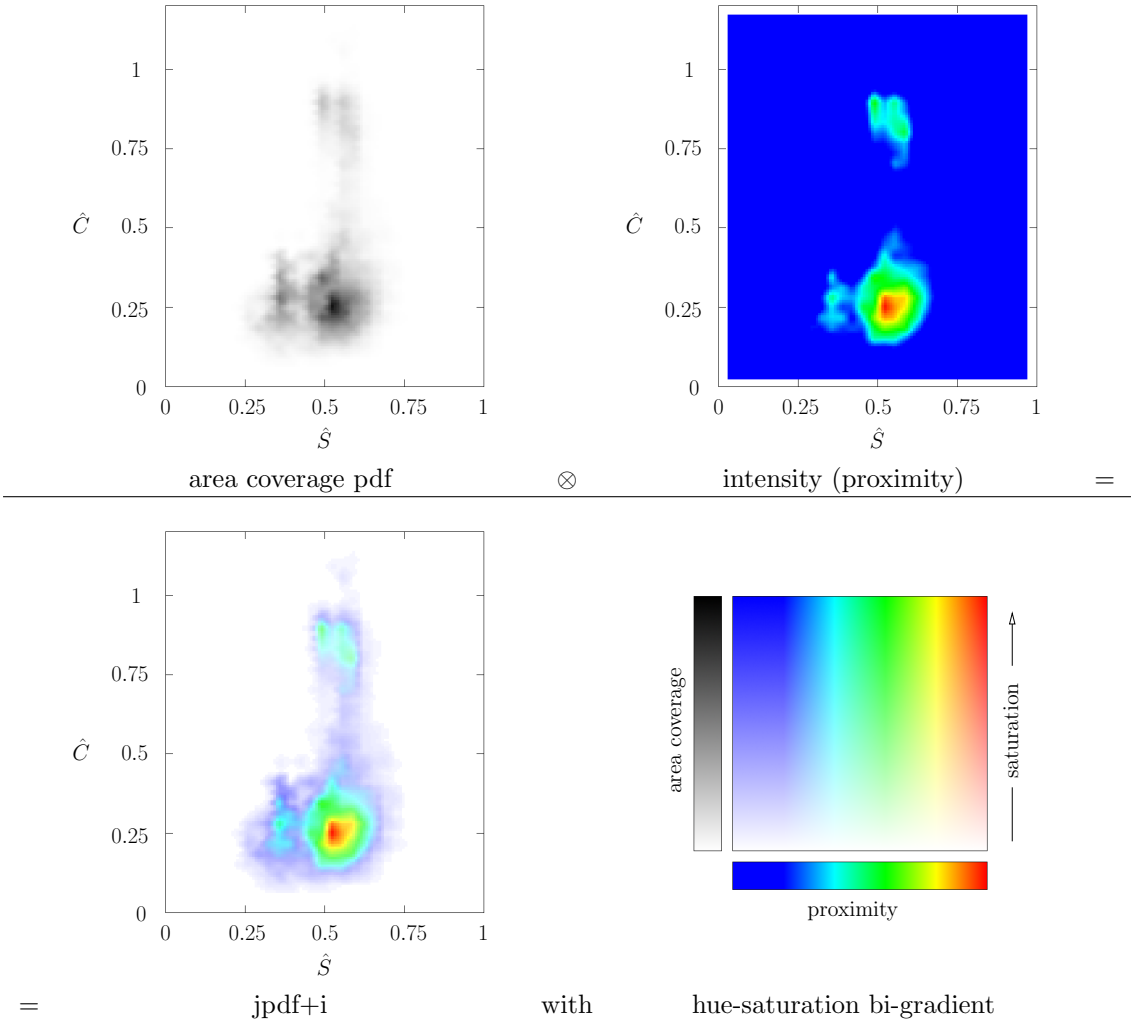

Figure 7.3: Components of the jpdf+i in terms of $(\hat{S}, \hat{C})$, plus intensity component based on proximity, of structures of $\mathcal{X}(Q) \cup \mathcal{X}([A_{ij}]_+)$ surrounding structures of $\mathcal{X}(Q)$: area-coverage pdf component (top left) using greyscale; intensity component (top right) using blue-cyan-green-yellow-red colorscale; composition of area-coverage pdf and intensity components to obtain the composite plot (bottom left) with bi-dimensional hue-saturation gradient scale (bottom right) corresponding to proximity (hue) and area coverage (saturation)

of structures of $\mathcal{A}$. Note that both scales are normalized: the maximum area coverage will have a saturated color, and red hue corresponds to the maximum proximity value. Therefore, they provide only relative (not absolute) information of the area coverage and the intensity (proximity) values. This can be changed fixing absolute ranges for the hue-saturation bi-gradient scale.

A first conclusion that can be directly drawn from Figure 7.3 is that structures of Q are mainly surrounded (more saturation), among those of $[A_{ij}]_+$ and Q itself, by structures with low values of $\hat{C}$, which are also closer (red hues). Those $\hat{C}$ values correspond to sheet-like structures. A desaturated

region (less area coverage) of also green/cyan hues (farther structures) is located nearer the $(\hat{S}, \hat{C}) \approx (1/2, 1)$ zone. This implies that, secondarily, tube-like structures surround also structures of Q, but they are not so proximal and cover a smaller relative surface area of them. When Figure 7.3 is compared to the right plot of Figure 6.4, since both share the same axes $(\hat{S}, \hat{C})$, it is indirectly concluded that the majority of sheet-like structures surrounding those of Q (as seen in Figure 7.3 by the saturated red-colored regions) are structures of $[A_{ij}]_+$ since they are the ones with a higher density of glyphs in the corresponding regions in the $(\hat{S}, \hat{C})$-plane of Figure 6.4.

7.3.2 Proximity split by groups through cumulative marginal pdfs

In Figure 7.4 we plot cumulative one-dimensional marginal pdfs obtained from $[\mathcal{P}(p,g)|_{\mathcal{A}\leftarrow B}$ for increasing group g numbers, $\{f_k(p) = \sum_{g=1}^{k} [\mathcal{P}(p,g)|_{\mathcal{A}\leftarrow B}, k = 1, ..., N_g\}$. The contribution of each group g is represented by a different color between black lines. For $k = N_g$, the result is the marginal pdf in terms of p, $f(p) = f_{N_g}(p)$, represented by a thicker black line.

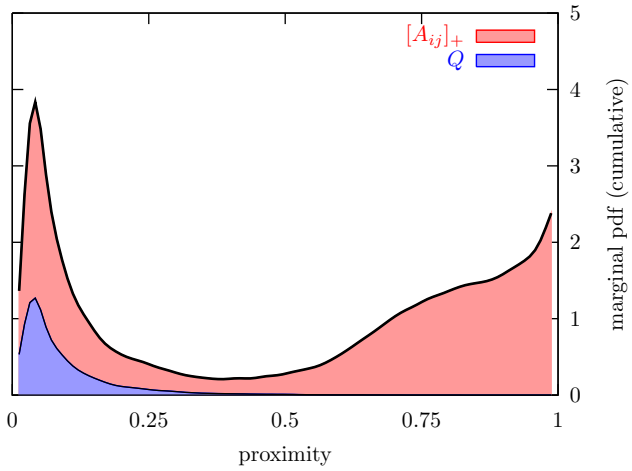

Figure 7.4: Representation of the marginal pdf of $[\mathcal{P}(p,g)|_{\mathcal{A}\leftarrow B}$ in terms of the proximity p (thick black line), showing the contribution of each group g by the different colored areas between two black lines (added cumulatively)

From Figure 7.4, it is directly concluded that structures of Q are predominantly surrounded by structures of $[A_{ij}]_+$, represented by the red area of the marginal pdf. The blue area corresponds to structures of Q, which cover a much smaller fraction and are farther (lower values of proximity) than those of the majority of $[A_{ij}]_+$ structures. This was indirectly concluded previously, from

the combination of Figures 7.3 and 6.4. The contribution of $[A_{ij}]_+$ (red area) to the marginal pdf in Figure 7.4 shows four regions of interest: first, the region near unitary proximity ($p \approx 1$), that corresponds to structures of $[A_{ij}]_+$ very close to those of Q, likely overlapping/intersecting each other. Examples of this interaction, extracted from the database under study, are shown in Figure 7.5, cases (a), (b), and (c). Second, the region with proximity values between 0.6 and 0.9, where a hump is visible in the marginal pdf, that corresponds to structures of $[A_{ij}]_+$ (or parts of them) still at a close distance but not overlapping or intersecting. Those values of proximity translate into distances between 1/10 and 2/3 times their own characteristic length, defined by μ, which corresponds, for the tube-like structures predominant in Q, to approximately 3/2 times their characteristic radius. See cases (d), (e), and sheets surrounding tubes in case (f) of Figure 7.5 for some examples of this configuration. Third, the region with proximity values between 0.25 and 0.5 with low values of the marginal pdf indicates that surrounding structures are rarely found at those distances. The fourth region corresponds to low values of proximity ($p \approx 0.1-0.2$). See, for example, tubes nearby other tubes in case (f) of Figure 7.5. As a result of the definition of p, a wide range of high values (> 4) of the relative distance between structures concentrates in that region, so it is expectable to find an accumulation of the marginal pdf for low p, whenever there are structures of $\mathcal{A}$ not completely surrounded by close ones of $\mathcal{B}$. A modification of the definition of p or the scale used to represent it can spread the effect of those higher distance over a wider range if required, but here we are more interested in closer structures, so the current p seems suitable for this purpose.

7.3.3 Structures of Q surrounding themselves

A question that arises after this analysis is whether structures of Q might be closer to themselves than what the blue region in Figure 7.4 shows, but structures of $[A_{ij}]_+$ eclipsing them when computing $\left[\vec{\mathcal{PI}}(\hat{S},\hat{C}\,;p)\right|_{\mathcal{A}\leftarrow\mathcal{B}}$ masquerade the result, making them appear farther than they are. This can be answered by applying the proposed methodology to $\mathcal{A} = \mathcal{B} = \mathcal{X}(Q)$, that is, considering the problem of how structures of Q surround themselves. Figure 7.6 shows the $\left[\vec{\mathcal{PI}}(\hat{S},\hat{C}\,;p)\right|_{\mathcal{A}\leftarrow\mathcal{B}}$ (left) and $[\mathcal{P}(p,g)|_{\mathcal{A}\leftarrow\mathcal{B}}$ (right) obtained in this case. Note that now there is only one group ($g = 1$).

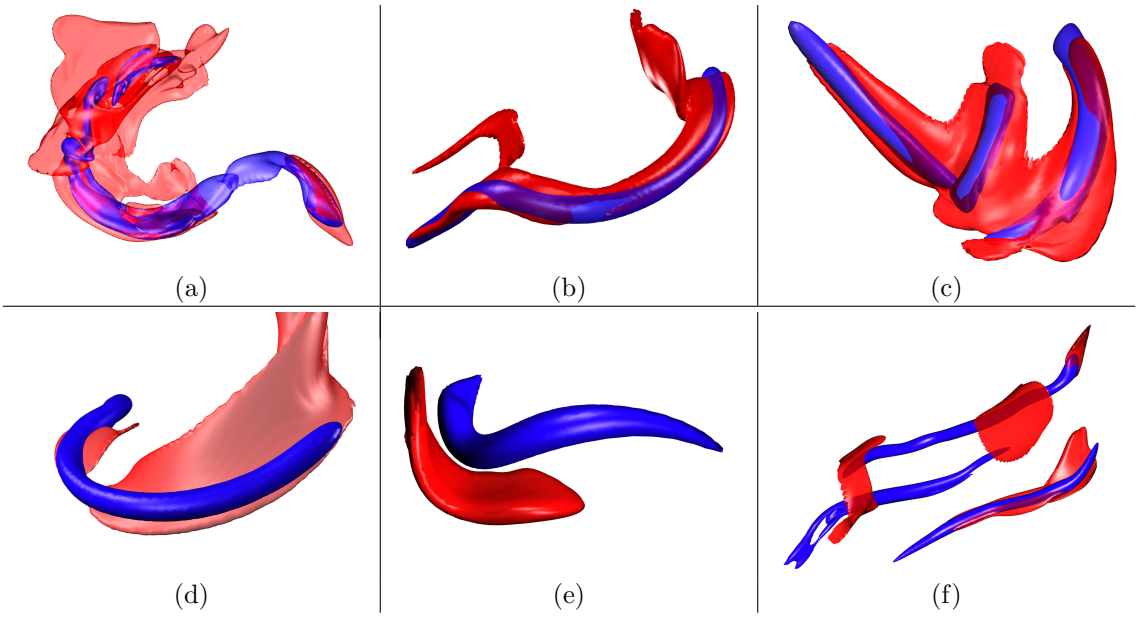

Figure 7.5: Examples of composite structures formed by interaction of tube-like (blue) and sheet-like (red) geometries found in the database. In cases (a) and (b) a tube is mostly embedded by one or more sheets that intersect it and remain at a close distance. Case (c) consists of three tubes and a sheet that follows closely their geometry, intersecting them, and connects them through stretched regions. Cases (d) and (e) show, each, a sheet-like structure wrapping around a tube, without intersecting it but remaining at a close distance and following its curvature. A smaller sheet intersecting the tube is also seen in case (d). Case (f) shows three tubes at moderate distances from each other ($\approx$ 5–10 times their average radius) with a similar orientation and sheets partially surrounding them at close distance or even intersecting them. For clarity, only a subset of all the nearby structures surrounding each tube in every case is shown

$\left[\vec{\mathcal{PI}}(\hat{S},\hat{C}\,;p)\right|_{\mathcal{A}\leftarrow\mathcal{B}}$ shows, as expected, tube-like geometries as the proximal, which is trivial once the sheet-like structures of $[A_{ij}]_+$ have been removed from $\mathcal{B}$. But $[\mathcal{P}(p,g)|_{\mathcal{A}\leftarrow\mathcal{B}}$ also shows a peak at about the same value of proximity that was found for Q structures when $[A_{ij}]_+$ structures were included, which confirms the farther distances among Q structures to themselves. See case (f) in Figure 7.5.

7.4 Application to structures of $\omega_i\omega_i$ and $S_{ij}S_{ij}$

Next we apply this methodology to structures of $\omega_i\omega_i$ and $S_{ij}S_{ij}$ educed in §5.3. For these two fields a multi-scale decomposition was performed. Of all possible combinations of fields and scales, we study two cases, due to their particular relevance. In both cases, we take $\mathcal{A}$ as the set of structures of $\omega_i\omega_i$ at scale number 3 (intermediate scale). They were found in §5.4 to be predominantly tube-

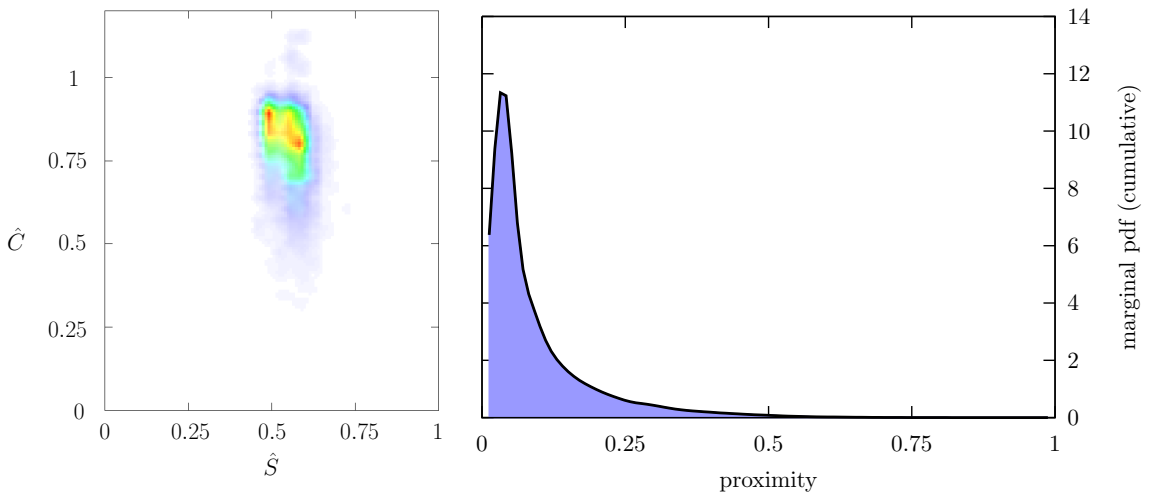

Figure 7.6: Results for structures of Q surrounding themselves: $\left[\vec{\mathcal{PI}}(\hat{S},\hat{C}\,;p)\right]\Big|_{\mathcal{A}\leftarrow\mathcal{B}}$ (left) $[\mathcal{P}(p,g)|_{\mathcal{A}\leftarrow\mathcal{B}}$ (right) for the case $\mathcal{A}=\mathcal{B}=\mathcal{X}(Q)$, $g=1$

like. We take $\mathcal{B}$ as the set of structures educed for scales numbers $3-6$ for $\omega_i\omega_i$ in the first case (thus, $\mathcal{A}\subset\mathcal{B}$) and for $S_{ij}S_{ij}$ in the second (thus, $\mathcal{A}\cap\mathcal{B}=\emptyset$). In both cases, we split $\mathcal{B}$ into four groups ($N_g=4$), each corresponding to a different scale number of the field under consideration ($\omega_i\omega_i$ or $S_{ij}S_{ij}$, respectively).

Figure 7.7 shows $\left[\vec{\mathcal{PI}}(\hat{S},\hat{C}\,;p)\right]\Big|_{\mathcal{A}\leftarrow\mathcal{B}}$ (left) and $[\mathcal{P}(p,g)|_{\mathcal{A}\leftarrow\mathcal{B}}$ (right), for the first (top) and second (bottom) cases. From the jpdf+i (left plots) it is observed that structures with small $\hat{C}$ (corresponding to sheet-like geometries) appear to be the closest in both cases (yellow and red spots). But there is a wide range of geometries among the surrounding structures.

In the first case, that is, for the set $\mathcal{B}$ containing structures of $\omega_i\omega_i$, two saturated regions (implying high area-coverage) are present in that plot, corresponding to tube-like (nearer the $(\hat{S},\hat{C})\approx(1/2,1)$ region) and sheet-like (small $\hat{C}$ values) structures. The latter appear closer (red and yellow hues, as opposed to green and cyan) but the former seem to cover a slightly higher percentage of the area of structures of $\mathcal{A}$ (more saturated colors). The region in between those two (intermediate values of $\hat{C}$) contains structures which appear farther and covering a smaller area.

In the second case, $\mathcal{B}$ containing $S_{ij}S_{ij}$ structures, the highest area-coverage corresponds clearly to those structures with low $\hat{C}$ (sheet-like), which are also the closest (red, yellow, and green hues). The spread toward other geometries is also significant, but the area-coverage and proximity decreases

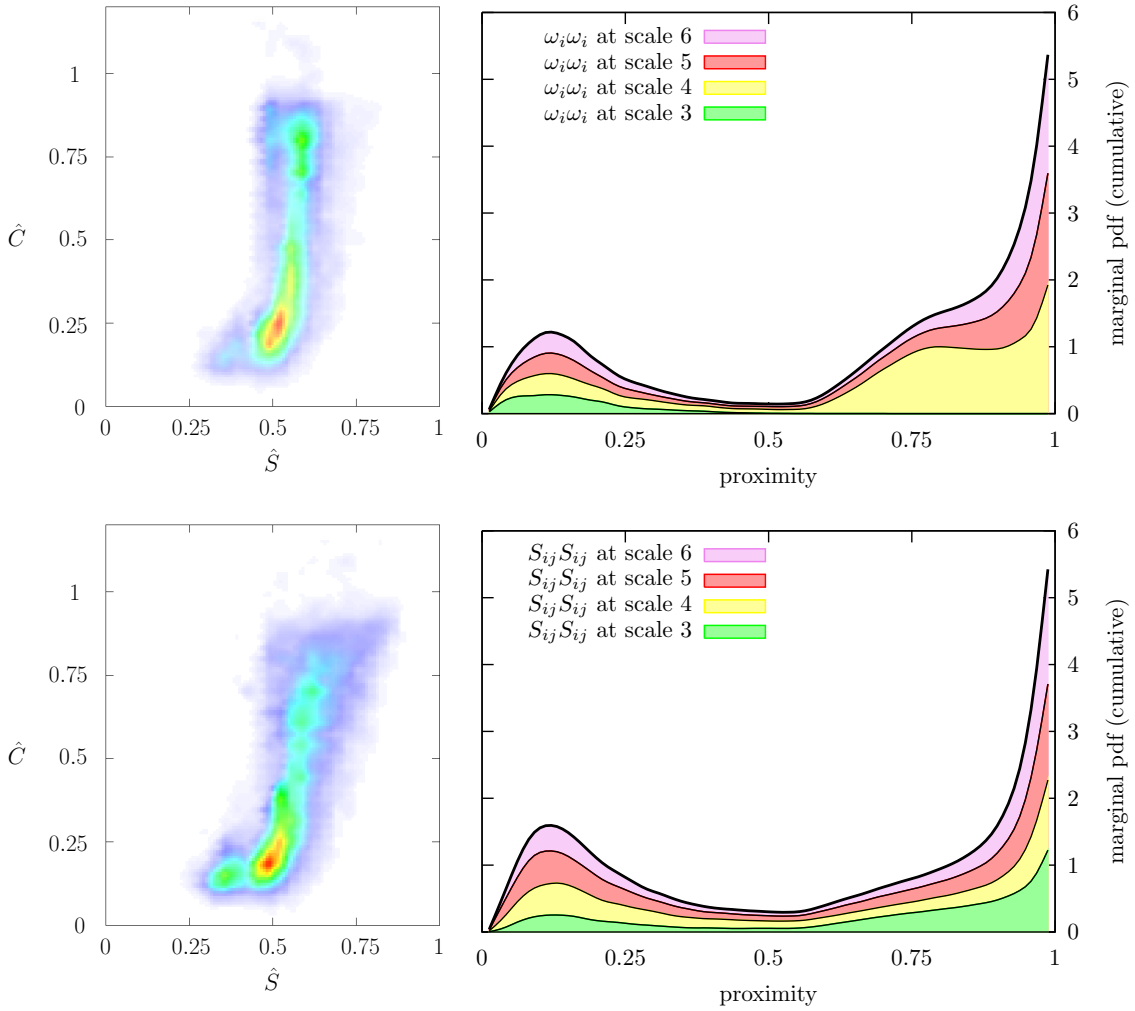

Figure 7.7: Results for structures of $\omega_i\omega_i$ at scale number 3 surrounded by structures of $\omega_i\omega_i$ (top) and by structures of $S_{ij}S_{ij}$ (bottom), at scale numbers $3-6$: $\left[\vec{\mathcal{PI}}(\hat{S},\hat{C}\,;p)\right|_{\mathcal{A}\leftarrow\mathcal{B}}$ (left) $[\mathcal{P}(p,g)|_{\mathcal{A}\leftarrow\mathcal{B}}$ (right)

in those other regions of the $(\hat{S},\hat{C})$-plane (less saturation and cyan and blue hues). Also, the region around tube-like structures found in the first case is now, in the second case, more diffuse and spread toward the blob-like region. This is consistent with the fact that less tubes were found in §5.3 in the geometrical analysis of structures of $S_{ij}S_{ij}$.

The right plots of Figure 7.7 show the cumulative marginal pdf obtained from $[\mathcal{P}(p,g)|_{\mathcal{A}\leftarrow\mathcal{B}}$, split by groups corresponding to each scale number under study (3 to 6). We use the same color code for each scale number as in Figures 5.7– 5.12 of Chapter 5. There are two main differences between both cases of study. In the first case, structures of $\omega_i\omega_i$ at scale number 3 have a small contribution

to the marginal pdf, and they appear far ($p \approx 0.1$), compared to the rest of the scales; structures at scale number 4 are the closest, showing a significant increase for p in the range 0.6-0.8, while structures at scale numbers 5 and 6 appear also close, but with a more gradual increase for $p > 0.6$. In the second case, structures of $S_{ij}S_{ij}$ at each one of the scales under analysis (3-6) have a more balanced contribution to the marginal pdf; scale number 3 shows a slightly higher concentration of closer structures ($p > 0.6$), and less proportion of farther structures ($p \approx 0.1$), when compared to structures at scale numbers 4–6.

7.5 Discussion

From this proximity study, tubes appear closely surrounded by sheets, both when structures of Q and those of an intermediate scale of $\omega_i\omega_i$ are analyzed, in relation to structures of $[A_{ij}]_+$ and the sets of structures of $\omega_i\omega_i$ and $S_{ij}S_{ij}$, respectively. Concerning structures of Q and $[A_{ij}]_+$ surrounding those of Q itself, it is found that a large proportion of structures of $[A_{ij}]_+$ appears much closer, with regions either intersecting or at less than one characteristic diameter of the tube-like structures of Q, and covering a larger proportion of their area than other surrounding structures of Q. These are, on average, farther than five diameters apart from themselves, as is also a second group of $[A_{ij}]_+$ structures, which might be surrounding those other Q structures at a closer distance.

Regarding structures of $\omega_i\omega_i$ at an intermediate scale (scale number 3), which were found to be predominantly tube-like in the previous geometrical study (see Chapter 5), we have considered the surrounding structures at the same and smaller scales (i.e., scale numbers from 3 to 6) of both $\omega_i\omega_i$ and $S_{ij}S_{ij}$, each field independently. In the first case, the set of structures of $\omega_i\omega_i$ at scale number 4 is the predominant group surrounding tubes of $\omega_i\omega_i$ at scale number 3. Structures of smaller scales (i.e., scale numbers 5 and 6) are also found close to those at scale number 3. In comparison, structures at scale number 3 appear farther among themselves. Concerning geometries of proximal structures, we find two predominant groups: sheet-like structures, which appear closer on average, and tube-like structures, certainly farther but with a high proportion of the total area-coverage. Other geometries, intermediate between tubes and sheets, had also a contribution, but to a lesser

degree of both proximity and area coverage.

In the second case, when structures of $S_{ij}S_{ij}$ at scale numbers 3–6 surrounding structures of $\omega_i\omega_i$ at scale number 3 are studied, all scales show similar results of proximity and area coverage. Structures at scale number 3 of $S_{ij}S_{ij}$ have a slightly higher value of proximity, likely owing to the similarity of some structures of both $\omega_i\omega_i$ and $S_{ij}S_{ij}$ at that intermediate scale. Regarding the geometry of proximal structures in this case, they are primarily sheet-like, with significantly higher proximity values and area-coverage. Other geometries can be seen among the surrounding structures but they tend more toward the region of blob-like structures, instead of tube-like structures, as opposed to the case of surrounding structures of $\omega_i\omega_i$ itself. Also, these other geometries are found farther and covering a smaller area fraction, on average.

Physically, these findings are consistent with the phenomenology of tubes being generated by one or multiple proximal sheets discussed in §5.6. Furthermore, as Ruetsch & Maxey (1992) pointed out when studying the evolution of small-scale structures in incompressible homogeneous isotropic turbulence, vortex tubes and vortex sheets should not be considered as separate, independent structures. Instead, they form composite structures, as those shown in Figure 7.5, with dependent geometries.

The results of this proximity analysis also support the structure-based explanation of intermittency, previously explored by Moisy & Jiménez (2004) using box counting methods. They found that intense structures form clusters of inertial-range extent. In our case, the low values of the cumulative marginal pdfs encountered for intermediate values of proximity suggest the existence of empty regions (in the iso-contour context) in physical domain in between composite structures.